Single-crystal synthesis and properties of the open-framework allotrope Si_{24}

Michael Guerette[a),1], Matthew D. Ward[1], Li Zhu, Timothy A. Strobel[a),1]

[1]Geophysical Laboratory, Carnegie Institution for Science, Washington, DC 20015, USA.

a) E-mail: mguerette@ciw.edu, tstrobel@ciw.edu

Received xxxxxx
Accepted for publication xxxxxx
Published xxxxxx

Abstract

Si_{24} is a new, open-framework silicon allotrope that is metastable at ambient conditions. Unlike diamond cubic silicon, which is an indirect-gap semiconductor, Si_{24} has a quasidirect gap near 1.4 eV, presenting new opportunities for optoelectronic and solar energy conversion devices. Previous studies indicate that Na can diffuse from micron-sized grains of a high-pressure Na_4Si_{24} precursor to create Si_{24} powders at ambient conditions. Remarkably, we demonstrate here that Na remains highly mobile within large (~100 μm) Na_4Si_{24} single crystals. Na readily diffuses out of Na_4Si_{24} crystals under vacuum with gentle heating (10^{-4} mbar at 125 °C) and can be further reacted with iodine to produce large Si_{24} crystals that are 99.9985 at% silicon, as measured by wavelength-dispersive X-ray spectroscopy. Si_{24} crystals display a sharp, direct optical absorption edge at 1.51(1) eV with an absorption coefficient near the band edge that is demonstrably greater than diamond cubic silicon. Temperature-dependent electrical transport measurements confirm the removal of Na from metallic Na_4Si_{24} to render single-crystalline semiconducting samples of Si_{24}. These optical and electrical measurements provide insights into key parameters such as the electron donor impurity level from residual Na, reduced electron mass, and electron relaxation time. Effective Na removal on bulk length scales and the high absorption coefficient of single-crystal Si_{24} indicate promise for use of this material in bulk and thin film forms with potential applications in optoelectronic technologies.

Keywords: silicon, allotrope, high-pressure precursor, optoelectronics, photovoltaic.

1. Introduction

Diamond cubic silicon (DC-Si, $Fd\bar{3}m$) is a foundation of modern technology, but the strongly indirect nature of the fundamental band gap ($E_{g,i}$ = 1.1 eV *vs*. $E_{g,d}$ = 3.4 eV)[1] places limitations on potential applications, for example, light absorption and emission processes [2–5]. New crystalline forms of silicon with novel properties are desirable for several reasons. As the second-most abundant element in the Earth's crust (behind oxygen), silicon is readily available and inexpensive. As the current microelectronics and photovoltaic industry standard, a mature infrastructure is built around the utilization and processing of silicon, and it is environmentally stable / non-toxic.

A variety of silicon allotropes are known under high-pressure conditions, and several persist at ambient conditions, as reviewed previously [6,7]. In brief, DC-Si undergoes a series of first-order phase transitions upon compression to form a series of metallic structures [8–14]. Upon release of

pressure (and subsequent heating), Si transforms to additional metastable structures depending on the specific processing path [15-22]. In addition, clathrate structures with multiple chemical species can also be treated to remove guest atoms from a host silicon lattice, leaving behind silicon frameworks such as Si_{136} [6,23,24]. Si_{136} possesses favorable optoelectronic properties with a direct (or nearly direct gap) near 1.9 eV [25–28], though some electronic dipole transitions are forbidden, which detracts from future possible applications [29]. Na diffusion is also extremely slow in Si_{136} because of the clathrate cage structure, making it difficult to obtain the necessary purity for semiconductor applications. Further barriers related to large-scale / film growth have inhibited subsequent developments of silicon clathrates [23,25,30]. Nevertheless, many other allotropes with novel optical properties are predicted with only slightly higher energies than the DC-Si [5,6,31–33], suggesting potential to access novel, metastable forms of silicon with favorable optoelectronic properties.

A novel open-framework allotrope of silicon, Si_{24}, was recently formed by a high-pressure precursor synthesis method [34,35]. Under this approach, the precursor phase (Na_4Si_{24}) is first prepared under high-temperature and high-pressure conditions (T ≈ 1123 K, P ≈ 9 GPa). This Na_4Si_{24} precursor has the $Eu_4Ga_8Ge_{16}$ (*Cmcm*) structure type [36], common for other alkaline- and rare-earth silicides, MSi_6 (M = Ca [37], Sr [38], Ba [39], Eu [40], Na [34,35]). The structure (with topology of calcium aluminosilicate zeolite (CAS) [41]) has a clathrate-like host lattice formed by sp^3–bonded silicon with five, six and eight-membered rings. Opposed to clathrates with polyhedral cages, Na_4Si_{24} contains channels along the crystallographic *a*-axis. The high-pressure Na_4Si_{24} precursor is next recovered to ambient conditions, and Na is removed to produce Si_{24}. The open channels in the structure facilitate Na mobility and removal [34,42]. Heating at 400 K under dynamic vacuum (10^{-5} mbar) was shown to reduce Na content to less than 0.1 at.% after eight days in multicrystalline samples with average grain sizes near 5 μm [34]. Thus, Si_{24} joins the short list of metastable Si allotropes that persist at ambient conditions.

Due to the nearly optimum band gap for a single *p-n* junction under the Shockley-Queisser limit (1.34 eV), Si_{24} represents a promising candidate to convert solar photons into electrical energy [34,43,44]. The quasidirect (nearly degenerate direct and indirect) band gap also means that less thermal energy is released upon electron-hole recombination. Thus Si_{24} could act as an efficient emitter of light for improved LED performance and optical communication, and could also allow additional transistors per chip in the quest for miniaturization through improved heat management. Overall, Si_{24} and other direct-gap forms of silicon have potential to broadly transform silicon-based optoelectronics. However, a lack of sizeable, high-purity crystals has prevented the characterization of intrinsic properties, which is the first step towards potential future applications.

Further potential applications for Si_{24} are indicated by doping studies using first-principles calculations. Formation energies for Si_{24} doped by group III and group V elements were found to be low, suggesting that *p*- and *n*-type Si_{24} and their junction are readily achievable. The dopants have low ionization energies and therefore can be easily ionized [43]. Calculations also indicate that the power factor of Si_{24} for *n*-type doping is always better than that for *p*-type samples for thermoelectric applications [45]. The electrochemical performance of Na_xSi_{24} was also investigated using density functional theory calculations, and the material was suggested as a potential anode for Na- or Li-ion batteries [42,46–48]. We note also that Arietta et al. predicted a metastable intermediate phase with composition $Na_{0.5}Si_{24}$ that could potentially hinder further Na removal [42].

Initial Na_4Si_{24} synthesis used powder Si mixed with elemental Na for a nearly homogeneous 1Na:6Si molar blend, then compressed and heated within a high-pressure multi-anvil apparatus [34],[35]. This approach typically produces dense multi-crystalline / powder Na_4Si_{24} pellets with DC-Si impurities. Recently, we used high-resolution transmission electron microscopy (HRTEM) to demonstrate that an epitaxial relationship exists between the DC-Si{111} and Na_4Si_{24} {113} planes, and large single crystals (mm scale) of Na_4Si_{24} can be grown by starting from large DC-Si crystals [49,50]. The single crystals of Na_4Si_{24} show high Na mobility, evident in electronic property measurements, suggesting that Na may be effectively removed from the Na_4Si_{24} structure on bulk length scales [50].

In this work, we demonstrate effective Na removal from the Na_4Si_{24} network on bulk length scales, leaving behind high-purity single crystals of Si_{24} up to 99.9985 at% Si. The resulting crystals represent doped semiconductors with approximately 10^{19} – 10^{20} free carriers/ cm^3. The availability of large single crystals allows us to characterize the semiconducting nature including the sharp direct-gap absorption edge with large absorption coefficient and electrical transport properties.

2. Methods

2.1 Synthesis and processing

As reported previously, single-crystalline Na_4Si_{24} was synthesized near 1123 K at 9 ± 0.5 GPa at the Geophysical Laboratory in a multi-anvil press via direct transformation of large pieces of intrinsic DC-Si (University Wafer) and Na metal pieces (Alfa 99.95%) [49,50]. Roughly 10-15 mg of Na and Si in approximate 1:6 molar ratio was prepared under an argon environment within a boron nitride (BN) capsule, which was then transferred into the multi-anvil assembly for synthesis. After a ~10 hour dwell time at the synthesis

conditions, the temperature was reduced at 1-3 K/min, and the pressure was decompressed at a rate of 0.7 GPa/hr. The recovered crystals were extracted from the BN capsule and sonicated in water. Typical runs resulted in a mixture of Na_4Si_{24} crystals (up to 500 μm in maximal dimension) and DC-Si crystals, which were easily separated under a microscope based on morphology and color.

Na was removed from recovered crystals via the thermal degassing process, which is summarized as follows [34,35]. Washed Na_4Si_{24} crystals were placed within a pouch made of 5 μm stainless steel mesh and either sealed in a quartz tube at 10^{-3} mbar or placed under dynamic vacuum at 10^{-5} mbar. Quartz tubes were then placed within a furnace operating between 398-573 K for 1-5 weeks. Additional Na removal was achieved through successive reactions with iodine. Iodine etching was previously used to remove Na from Na_xSi_{136} to produce Si_{136}, a much more difficult structure from which to remove sodium due to the cage enclosure of Si around Na requiring temperatures of 573 K – 673 K [24]. Here, Na_4Si_{24} single crystals were sealed with iodine crystals in quartz tubes. The quartz tube was immersed in liquid nitrogen to prevent iodine sublimation, placed under vacuum of 4×10^{-3} mbar, and flame sealed with a H_2/O_2 torch. Sealed tubes were then heated at 398 K or 573 K for 1-5 weeks.

2.2 X-ray diffraction

Powder / multi-crystalline X-ray diffraction (PXRD) was used to monitor relative phase fractions in response to Na removal over time (see *Supporting Information*). Data were acquired on a Bruker D8 Discover diffractometer with a Cu K_α (λ = 1.5406 Å) microfocus source and Vantec 500 area detector. Phase identification and phase weight fraction refinements were conducted with the JADE software [51].

Single-crystal X-ray diffraction (SXRD) of Si_{24} was conducted at 100 K using a Bruker APEX diffractometer equipped with graphite-monochromatized Mo K_α (λ = 0.71073 Å) radiation. A blocky Si_{24} crystal with parallel faces and dimensions 174 μm × 100 μm × 52 μm was mounted for SXRD. The crystal-to-detector distance was set to 60 mm and data were collected with an exposure time of 10 s/frame. The APEX3 program was used for the collection and reduction of intensity data and for cell refinement. Data were collected as a series of 0.5° scans in θ and ω [52]. The program SADABS [53] was utilized for face-indexed absorption, incident beam, and decay corrections. The SHELX-14 suite of programs was used for structure solution and refinement [54,55]. Atom position standardization was performed using the program STRUCTURE TIDY [56,57]. Crystallographic images were created using the program CRYSTALMAKER [58]. CSD 1965259 contains supplementary crystallographic data for this paper. These data can be obtained free of charge from the joint CCDC's and FIZ Karlsruhe's service to view and retrieve structures via https://www.ccdc.cam.ac.uk/structures/.

In situ temperature-dependent X-ray diffraction patterns of a Si_{24} single crystal were collected at the Advanced Photon Source, Sector 13, GSECARS using a monochromatic wavelength of 0.3344 Å. The X-ray beam was focused on the sample to a size of ~3 μm and scattered X-rays were detected using a PILATUS 1M detector, calibrated with a LaB_6 standard and the program DIOPTAS.[59] The sample was held in a diamond anvil cell (DAC) for convenience, with no applied pressure. Resistive heating was achieved by a ceramic heating element. Temperature was monitored with a Type K butt-welded thermocouple cemented against the diamond which supported the sample. Due to geometrical restrictions, only the (0 2 0), (0 2 3) and (2 0 0) reflections were monitored and fit with Gaussian peak shapes to determine the lattice parameters as a function of temperature (See *Supporting Information*).

2.3 Electron microscopy / spectroscopy

Scanning electron microscopy (SEM) imaging was performed on a JEOL JSM-6500F scanning electron microscope (SEM). Electron backscatter diffraction (EBSD) patterns were collected using an Nordlys Nano EBSD camera from Oxford. Samples were tilted so that the surface normal was 70° from the incident electron beam and the detector angle was at 90°. Energy-dispersive X-ray spectra (EDXS) were collected using an Oxford Instruments X-max detector with 80 mm^2 area. All samples were plasma-coated with a thin film of Ir (approximately 10 Å) to minimize electrical charging during EDXS and EBSD measurements. The Aztec software[60] was used for EBSD and EDXS data analysis.

Quantitative sodium concentration measurements within Si_{24} were performed by wavelength-dispersive spectroscopy (WDS) using the JEOL 8530F Hyperprobe at the Geophysical Laboratory. Analyses were performed at 10 kV and 60 nA on unmounted cleaved crystals placed on an Al stub and plasma-coated with approximately 10 Å of Ir to match the standard. A basalt glass standard was used to determine Na and Si concentration by 30 s peak and background collection, giving a Na detection accuracy of ±34 ppm.

2.3 Optical and electrical measurements

Optical absorption measurements were made with a Bruker Vertex 70 FTIR system in conjunction with a Hyperion microscope utilizing reflecting objectives. A single crystal of Si_{24} with parallel faces (lateral dimensions >50 μm) and likely orientation of [001] normal (based on cleavage described below) was supported by a ~50 μm pinhole for measurement in air. The thickness (t) was determined to be 11.8 μm, using interference fringes in the spectrum of transmitted light in the region of 0.8 eV (6450 cm^{-1}) with the relation

$$t = \frac{N}{2 \cdot n \cdot \Delta\lambda}, \quad (1)$$

where n is the refractive index and N is the number of fringes within spectral range $\Delta\lambda$ (in cm^{-1}). To estimate n, we used density functional theory (DFT) calculation to obtain the frequency-dependent complex dielectric function. The real (ϵ_1) and imaginary parts (ϵ_2) of the dielectric function are related to the refractive index by

$$n = \frac{1}{\sqrt{2}}\sqrt{\epsilon_1 + \sqrt{\epsilon_1 + \epsilon_2}}. \quad (2)$$

Quantitative absorption coefficient (α) values were obtained by measuring reflection (R) and transmission (Tr) spectra of the crystal and by inverting the equation

$$Tr = \frac{(1-R)^2 exp(-\alpha t)}{1-R^2 exp(-2\alpha t)}. \quad (3)$$

The temperature dependence of the electrical resistivity, $\rho(T)$, was measured using a Keithley 2400 sourcemeter in two-probe geometry, in conjunction with an open-flow cryostat used to cool the sample to 77 K with measurements recorded every ~5 K upon warming. Electrical leads composed of W_xC_{1-x} were deposited using a FEI Helios G4 PFIB, a dual beam Xe^+ plasma FIB/SEM. The sample was first coated with Ir to prevent charging, and the Ir was removed with the Xe^+ ions with an 8 kV acceleration voltage to prevent significant amorphization of the surface layer. Contacts were also deposited at 8 kV. For the dimensions of the sample contacts, the contributed resistivity is on the order of 2-3 Ω, which is negligible compared to the sample resistance. Generally non-Ohmic behavior was observed, though non-rectifying and linear (Ohmic) in the region near V=0. Similar behavior in this low-voltage region has been reported previously for other semiconductors with FIB-deposited contacts.[61,62] Resistivity with temperature, $\rho(T)$, data were taken with 10 μA source current in 2-point configuration, requiring $0.1 < V < 0.4$. Within this range, the I-V curve can be approximated as linear which brings confidence to our relative measurements (approximating Ohmic contacts, see *Supporting Information*).

2.4 Computational methods

Ab initio structural relaxation was performed using density functional theory within the Perdew-Burke-Ernzerhof parametrization [63] of generalized gradient approximation [64] as implemented in the VASP (Vienna Ab Initio simulation package) code [65]. The Heyd-Scuseria-Ernzerhof hybrid functional (HSE06) [66,67] was used to estimate the dielectric response with reference to conventional unit cell directions (*Supporting Information*). The projector augmented wave (PAW) method [68] was adopted with the PAW potentials taken from the VASP library where $3s^2 3p^2$ was treated as valence electrons for Si atoms. The use of the plane-wave kinetic energy cutoff of 400 eV, adopted here, was shown to give excellent convergence of total energies. The frequency-dependent dielectric tensor was calculated using the independent-particle approximation [69] implemented in the VASP code [65].

3. Results and Discussion

After the thermal degassing of Na from Na_4Si_{24} to obtain Si_{24}, many flat and thin crystals are recovered after sonication in water (e.g., Figure 1A). A significant change in lattice parameters by XRD serves as the preliminary diagnostic for Na removal. Electron backscatter diffraction (EBSD, Figure 1C) analysis of several Si_{24} crystals with the same general morphology (flat, thin, shiny, slight bluish hue) reveal a common orientation with the crystallographic *c*-axis perpendicular to the lateral plane, i.e., [001] normal (Figure 1D). This observation indicates a preferential cleavage habit along the *a*-*b* plane. The cleavage produces flat crystals with near-parallel faces and allows for high-quality EBSD patterns without sample preparation. When considering the crystal structure, fracture along the *a*-*b* plane can be an expected means of stress relief because of the low energy associated with creating surfaces with this orientation (i.e., the plane with lowest bond density), as indicated by the dashed line in Figure 1E. Because most Si_{24} crystals have this fracture habit, subsequent optical and electrical transport measurements were performed on crystals with such an orientation.

The [001] orientation indicates that the channels along the *a*-axis, which host the Na ions in Na_4Si_{24}, are not aligned with the thinnest dimension of the crystal. Given that recovered Si_{24} crystals contain minimal Na (as described in detail below), the observed orientation reveals that sodium ions remain mobile along the greatest lateral dimensions of the crystals and can diffuse over bulk length scales (i.e., mm scale). Previous diffusion was observed on the scale of ca. 5 μm [34,35]. First-principles calculations indicate that Na diffusion and electrical transport are both greatest along the *a*-axis [42,45,70].

Careful inspection of the microstructure of Si_{24} crystals reveals pitting / micro-cracking on the cleaved surface (Figure 1B). Due to the observation of sharp SXRD spots with very low mosaic spread ($\Delta\omega \sim 0.5°$), we do not believe that these defects propagate into the bulk of the particular crystal shown in Figure 1B. However, FIB cross sections on multiple recovered crystals do indicate the tendency to form micro-cracks in the *a*-*c* / *b*-*c* planes, in addition to the natural cleavage along *a*-*b*. Na removal imparts significant anisotropic lattice strain upon conversion of Na_4Si_{24} to Si_{24}. [34] After Na removal, the change in lattice parameters are: Δa = -0.265 Å (-6.5%,), Δb = +0.112 Å (+1.1%), and Δc = +0.349 Å (+2.8%).

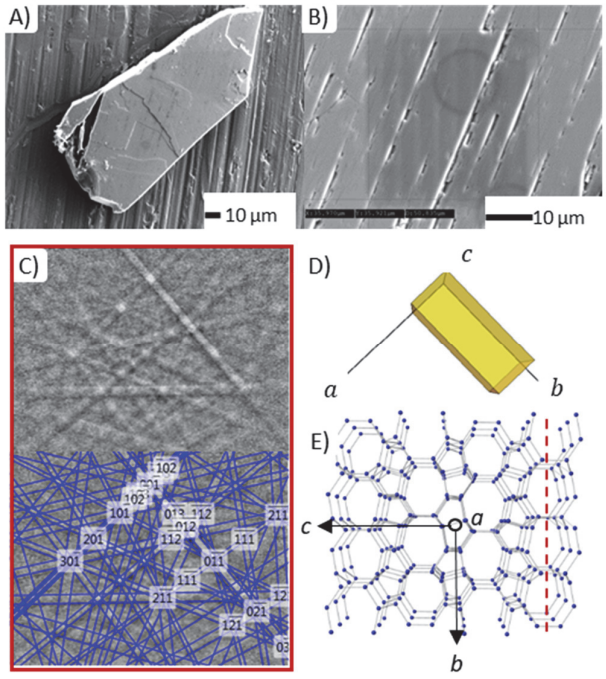

Figure 1. A) SEM image of Si_{24} single crystal with [001] normal to the imaged surface. WDS and SXRD were both conducted on this crystal. B) A closer view of the crystal in A) reveals micro-cracking. C) EBSD pattern of cleaved Si_{24} surface with [001] normal. D) Orientation observed for multiple flat / thin Si_{24} crystals with common cleavage habit with *c*-axis normal (as pictured A). E) Si_{24} crystal structure showing low-energy cleavage plane (red dashed line).

Significant anisotropic strain likely facilitates the propagation of cracks and is considered to be the primary cause for the observed micro-cracking. Temperature also exacerbates the micro-cracking, as much more significant cracking is observed for crystals treated at 573 K than those treated at 398 K (Figure S3). In situ, high-temperature XRD results of a Si_{24} single crystal reveal that the *a* and *c* axes expand, while the *b*-axis contracts with increasing temperature (Figures S2). Compared to the lattice distortions that accompany Na removal, these thermal changes are minor, but may also contribute to cracking. Thus a balance exists between temperature conditions for Na removal and crystal quality. While increased T provides thermal energy for Na diffusion (and shorter degassing times), lower-temperature conditions (≤ 400 K) appear favorable for producing higher-quality Si_{24} crystals.

The quantitative residual sodium concentration within Si_{24} crystals was determined by WDS. Typical crystals treated under vacuum at 398 K for > 1 week exhibit Na concentrations <0.1 at%, similar to previous results on powder samples [34]. While WDS penetration depth is limited to few microns below the surface, higher acceleration voltages were avoided due to concern for converting the Si_{24} structure to DC-Si. Subsequent reaction with I_2 significantly reduces the Na concentration, as shown previously for Si_{136} clathrate [24]. The lowest Na content observed was from a crystal treated in an iodine atmosphere at 398 K for ~5 weeks. In this case, WDS measurements revealed a maximum Si purity of 99.9985 at% (15 ppm Na, ca. $Na_{0.0003}Si_{24}$), which is at the detection limit of the instrument, as shown in Table 1.

Table 1. Na concentration from WDS (minimum, average < >, and standard deviation σ) after iodine reaction at 398 K for different times. The crystal shown in Figure 1 was treated for 820h.

Time (h)	Measurements	Min. Na (at%)	<Na> (at%)	σ_{Na} (at%)
182-210	23	0.0026	0.018309	0.01128
820	22	0.0015	0.013964	0.008739

The structure of the low-Na Si_{24} crystal (from Figure 1 and Table 2) was determined by SXRD. As mentioned above, the diffraction quality of this crystal was high and it produced sharp, symmetric spots that did not typically extend beyond two frames with an ω step size of 0.5°. The structural refinement at 100 K reproduces the experimental observations with exceptional agreement (R_1 = 1.34%, Table S1). Notably, no residual electron density from sodium was observed (maximum (F_{obs} - F_{calc}) = 0.27 $e^-/Å^3$). The lattice parameters of single-crystalline Si_{24} agree with previous powder observations after accounting for differences in measurement temperature [34]. The high-quality, single-crystal structure provides precise Si–Si bond distances and Si–Si–Si angles, which range from 2.3433(3)–2.3740(7) Å and 93.839(19)–135.828(19)°, respectively, at 100 K.

Table 2. Crystallographic data for Si_{24} at 100 K.

Crystal System	Orthorhombic
Space Group	*Cmcm*
a / Å	3.815(1)
b/ Å	10.684(1)
c / Å	12.628(1)
V / $Å^3$	514.648(4)
Z (Si_6)	4
Density, ρ_{calc} (g/cm^3)	2.175
T /K	100 (2)
Absorption Coefficient (mm^{-1})	1.446
Reflections Collected	3044
Data/Parameters/Restraints	466/19/0
Data Completeness	1.000
R_{int}	0.0206
$R(F)$ [I > 2σ(I)][a]	0.0134
$R_w(F_o^2)$[b]	0.0330

[a] $R(F) = \sum||F_o|-|F_c||/\sum|F_o|$ for $F_o^2 > 2\sigma(F_o^2)$. [b] $R_w(F_o^2) = \{\sum[w(F_o^2-F_c^2)^2]/\sum wF_o^4\}^{½}$ for all data. $w^{-1} = \sigma^2(F_o^2) + (0.0121F_o^2)^2$ for $F_o^2 \geq 0$; $w^{-1} = \sigma^2(F_o^2)$ for $F_o^2 < 0$.

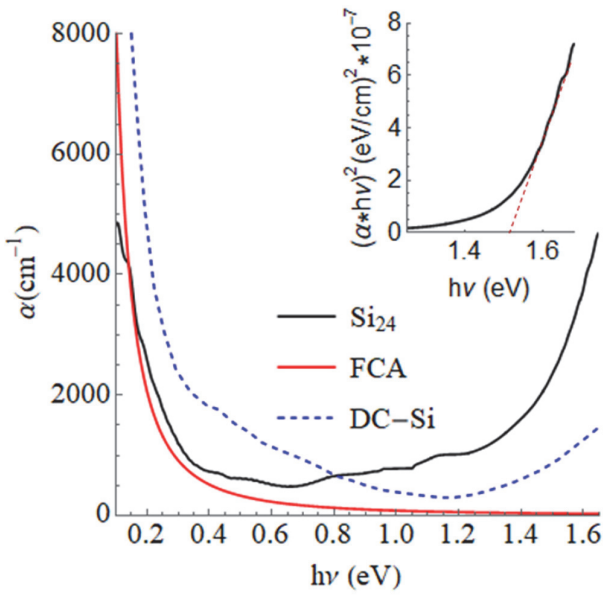

Figure 2. Optical absorption of single-crystalline Si_{24}. For comparison, arsenic-doped DC-Si with $n_{As} = 4 \times 10^{19}$ cm^{-3} is presented (dashed line). [71,72] Mid-infrared free carrier absorption (FCA) from the Drude model (Eq. (4)) is also shown, with parameters: $m^* = 0.23m_e$, $n_e = 7\times10^{19}$, $\tau = 5\times10^{-15}$ s, and $n = 3.05$. Inset: Tauc plot analysis for a direct-gap semiconductor with band gap of 1.51(1) eV.

Thin Si_{24} crystals with near-parallel faces were selected for optical absorption measurements (presumably oriented along [001] as the optical axis). A representative absorption spectrum of Si_{24} is compared with arsenic-doped DC-Si with $n_{As} = 4\times10^{19}$ cm^{-3} [71] in Figure 2. The spectrum is characterized by three distinct absorption phenomena in different photon energy regimes (discussed below), as is typical for doped semiconductors.[72,73] At higher energy (near 1.4-1.5 eV) a steep increase in the absorption coefficient represents the optical gap. Compared to DC-Si, Si_{24} exhibits a significantly enhanced absorption coefficient near the band edge (e.g., >3× at 1.65 eV), which allows for high absorption of visible light and the majority of solar spectral irradiation. The data indicate absorption coefficient above the band edge of ~5.0 × 10^3 cm^{-1} at 1.65 eV. From the Beer Lambert law, a film thickness of 10 μm should result in 95% light absorption at this energy. The observable magnitude of higher-energy absorption of Figure 2 is limited by the transmission geometry, however, DFT calculations predict absorption values continue to rise dramatically with energy (Figure S4).

The Tauc plot [74,75] of $(\alpha h\nu)^2$ vs. $h\nu$ yields a straight line that extrapolates to 1.51(1) eV at $\alpha = 0$, thus representing the value of the direct band gap $E_{g,d}$ (Figure 2, inset). Previous measurement of powdered material revealed a direct transition at 1.39 eV [34]. The increased value of the band gap observed here may be the result of decreased dopant levels in the Si_{24} structure. [76,77]

Similar to other desodiated clathrate materials, [30,78–80] the low-energy, mid-infrared region of the spectrum is dominated by free carrier absorption (FCA), as shown in Figure 2. This behavior indicates a sufficient number of free carriers (residual electrons from Na) that can undergo intraband transitions via absorption of infrared light. For doped DC-Si, FCA is observed at carrier concentrations as low as 10^{16} cm^{-3} in *n*-type silicon.[72] In order to estimate physical parameters of the Si_{24} sample, we applied the Drude model [81], where the absorption coefficient from free carriers is given by

$$\alpha(E) = \frac{n_e e^2}{4\pi\epsilon_o cnm^*\tau\left(\frac{E}{\hbar}\right)^2}, \quad (4)$$

where n_e is the number of free electrons per unit volume, e is the electron unit charge, ϵ_o is the permittivity of free space, c is the speed of light, n is the refractive index, m^* is the reduced electron mass, and τ is the electron relaxation time. We estimate that $n = 3.05$ from DFT calculations of optical constants (see *Supporting Information*), and that $m^* = 0.23m_e$ from the slope of ρ(T) (see below). Assuming that all carriers originate from Na, we estimate the minimum carrier concentration from WDS measurements. Given that the density of Si_{24} is 2.175 g/cm^3 (at 100 K), this translates to a reduced atomic density of 4.66×10^{22} Si atoms / cm^3 compared with 4.99×10^{22} Si atoms / cm^3 for DC-Si. Presuming a silicon purity of 99.9985 at%, a minimum carrier concentration of $n_e = 7\times10^{19}$ Na atoms / cm^3 is expected, neglecting atomic weight differences. Using these values for the measured sample we estimate a scattering relaxation time of $\tau = 5\times10^{-15}$ s (Figure 2B). This value is roughly an order of magnitude lower than for *n*-type DC-Si with somewhat lower doping of $n_e = 3.6\times10^{18}$, [82] and may also have considerable directional dependence.

In the intermediate energy regime near 1 eV, another mechanism gives rise to absorbance on the order of 1×10^3 cm^{-1}. This absorption regime can be clearly seen before the optical gap by subtracting the FCA contribution (Figure 2). This additional absorption regime is commonly observed for *n*-type silicon and GaAs,[72,73,76] and is similarly attributed to transitions within the conduction band.[72]

Temperature-dependent electrical transport measurements were conducted with two of four linear probes (Figure 3). The resistivity was calculated according to $\rho = \frac{wt}{s}\mathsf{R}$, where w and s are defined in Figure 3A, $t = 10 \pm 1$ μm thickness, and R is the measured resistance. The electrical conductivity increases with temperature, reflecting the behavior of a doped semiconductor rather than the metallic behavior of Na_4Si_{24},[50] and is similar to doped DC-Si.[83] For DC-Si with 10^{18} donors/cm^3, full donor ionization at 300 K is reduced

by 50% at 100 K, so thermal ionization dependence can account for much of the conductivity behavior in our sample.[83] Treating Si_{24} as a semiconductor with impurity donors, the extrinsic electrical conductivity is proportional to temperature by

$$\ln \sigma \propto -(E_g - E_d)/2k_BT, \quad (5)$$

where E_g is the band gap energy, E_d is the donor level energy, and k_B is Boltzmann's constant. Here, the energy of impurity ionization $E_i = E_g - E_d = 0.032$ eV, reveals a donor level energy of $E_d = 1.48(1)$ eV. Linear, non-rectifying behavior in the I-V region used for these measurements assures confidence in these relative measurements.

The energy of impurity ionization (E_i) also allows us to estimate the effective electron mass (m^*) through the relation

$$E_i = \frac{m^* e^4}{8\varepsilon^2 h^2}, \quad (6)$$

where $\varepsilon = 10\varepsilon_0$ represents the static dielectric constant for Si_{24} (estimated from Figure S4), and h is Planck's constant. By this treatment, $m^* = 0.23m_e$. This value is used to constrain the Drude model for free carrier optical measurement as described previously. By comparison, $m^* = 0.27m_e$ for n-type DC-Si with $n_e = 3.6\times10^{18}$ [82]. Additional details can be found in the *Supporting Information.*

4. Conclusion

In conclusion, large single crystals (>100 μm) of Si_{24} have been obtained by successful Na removal from large Na_4Si_{24} single crystals. Desodiation of the parent phase results in Si_{24} crystals with relatively low impurity content (Na ≤ 0.0015 at%). The strain associated with Na removal and thermal treatment may result in cleavage along the *a-b* plane and degraded crystal quality, particularly at temperatures above ca. 400 K. Quantitative optical absorption measurements on low-Na single-crystalline Si_{24} show a direct transition at 1.51(1) eV, and a significantly increased absorption coefficient compared with DC-Si. The spectrum at low energy is dominated by absorption from free carriers. Electrical transport measurements confirm the semiconducting nature of Si_{24} samples and reveal a substantial number of residual carriers, which help to constrain the donor ionization energy and effective mass. Successful Na removal on bulk length scales results in the production of bulk, single-crystalline *n*-type Si_{24}. Additional doping strategies may result in the creation of *p*-type material, and the possibility for intrinsic material via inert atom doping [84] remains a future possibility. The prospect of large single crystals, combined with unique physical properties including a high absorption coefficient, justify further research endeavors on this material, which may enable future synthetic strategies under practical conditions.

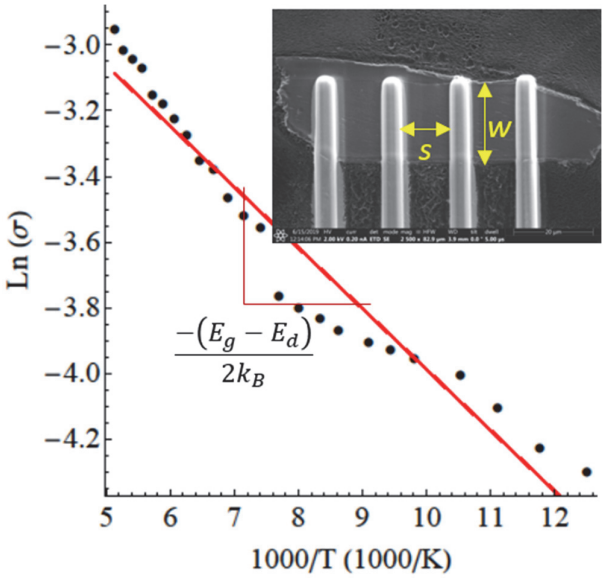

Figure 3. ρ(T) response in the extrinsic region where the slope reveals the impurity ionization energy. Linear leads were deposited on a Si_{24} sample for resistivity measurements (inset).

Acknowledgements

We thank J. Bertke for use of the X-ray Diffraction Facility at the Department of Chemistry, Georgetown University; Y. Fei for guidance and use of multi-anvil facilities at the Geophysical Laboratory; E. Bullock and S. Vitali at the Geophysical Laboratory for help with the microprobe and FIB instruments; E. Greenberg and V. Prakapenka at Center for Advanced Radiation Sources, University of Chicago, Chicago, IL 60637, USA. This work was supported by Energy Frontier Research in Extreme Environments (EFree) Center, an Energy Frontier Research Center funded by the US Department of Energy, Office of Science under award number DE-SC0001057 and the National Science Foundation, Division of Material Research (NSF-DMR) under award number 1809756. Portions of this work were performed at GeoSoilEnviroCARS (The University of Chicago, Sector 13), Advanced Photon Source (APS), Argonne National Laboratory. GeoSoilEnviroCARS is supported by the National Science Foundation – Earth Sciences (EAR – 1634415) and Department of Energy- GeoSciences (DE-FG02-94ER14466). This research used resources of the Advanced Photon Source, a U.S. Department of Energy (DOE) Office of Science User Facility operated for the DOE Office of Science by Argonne National Laboratory under Contract No. DE-AC02-06CH11357.

References

[1] Yoo W S, Kang K, Murai G and Yoshimoto M 2015 Temperature Dependence of Photoluminescence Spectra from Crystalline Silicon *ECS J. Solid State Sci. Technol.* **4** P456–61

[2] Ng W L, Lourenco M A, Gwilliam R M, Ledain S, Shao G and Homewood K P 2001 An efficient room-temperature silicon-based light-emitting diode *Nature* **410** 192

[3] Theis T N and Solomon P M 2010 It's time to reinvent the transistor! *Science* **327** 1600–1601

[4] Fujita M 2013 Silicon photonics: Nanocavity brightens silicon *Nat. Photonics* **7**

[5] Botti S, Flores-Livas J A, Amsler M, Goedecker S and Marques M A 2012 Low-energy silicon allotropes with strong absorption in the visible for photovoltaic applications *Phys. Rev. B* **86** 121204

[6] Haberl B, Strobel T A and Bradby J E 2016 Pathways to exotic metastable silicon allotropes *Appl. Phys. Rev.* **3** 040808

[7] Tonkov E Y and Ponyatovsky E G 2004 *Phase transformations of elements under high pressure* vol 4 (CRC press)

[8] Gupta M C and Ruoff A L 1980 Static compression of silicon in the [100] and in the [111] directions *J. Appl. Phys.* **51** 1072–5

[9] Olijnyk H, Sikka S K and Holzapfel W B 1984 Structural phase transitions in Si and Ge under pressures up to 50 GPa *Phys. Lett. A* **103** 137–40

[10] Hu J Z, Merkle L D, Menoni C S and Spain I L 1986 Crystal data for high-pressure phases of silicon *Phys. Rev. B* **34** 4679–84

[11] Sorella S, Casula M, Spanu L and Dal Corso A 2011 Ab initio calculations for the β-tin diamond transition in silicon: Comparing theories with experiments *Phys. Rev. B* **83** 075119

[12] Purwanto W, Krakauer H and Zhang S 2009 Pressure-induced diamond to beta-tin transition in bulk silicon: a near-exact quantum Monte Carlo study *Phys. Rev. B* **80**

[13] McMahon M I and Nelmes R J 1993 New high-pressure phase of Si *Phys. Rev. B* **47** 8337–40

[14] McMahon M I, Nelmes R J, Wright N G and Allan D R 1994 Pressure dependence of the Imma phase of silicon *Phys. Rev. B* **50** 739–43

[15] Kasper J S and Richards S M 1964 The crystal structures of new forms of silicon and germanium *Acta Crystallogr.* **17** 752–5

[16] Crain J, Ackland G J, Maclean J R, Piltz R O, Hatton P D and Pawley G S 1994 Reversible pressure-induced structural transitions between metastable phases of silicon *Phys. Rev. B* **50** 13043–6

[17] Zhao Y-X, Buehler F, Sites J R and Spain I L 1986 New metastable phases of silicon *Solid State Commun.* **59** 679–82

[18] Weill G, Mansot J L, Sagon G, Carlone C and Besson J M 1989 Characterisation of Si III and Si IV, metastable forms of silicon at ambient pressure *Semicond. Sci. Technol.* **4** 280

[19] Wentorf R H and Kasper J S 1963 Two New Forms of Silicon *Science* **139** 338–9

[20] Besson J M, Mokhtari E H, Gonzalez J and Weill G 1987 Electrical properties of semimetallic silicon III and semiconductive silicon IV at ambient pressure *Phys. Rev. Lett.* **59** 473–6

[21] Kobliska R J and Solin S A 1973 Raman Spectrum of Wurtzite Silicon *Phys. Rev. B* **8** 3799–802

[22] Pandolfi S, Renero-Lecuna C, Godec Y L, Baptiste B, Menguy N, Lazzeri M, Gervais C, Spektor K, Crichton W A and Kurakevych O O 2018 Nature of Hexagonal Silicon Forming via High-Pressure Synthesis: Nanostructured Hexagonal 4H Polytype *Nano Lett.*

[23] Krishna L, Baranowski L L, Martinez A D, Koh C A, Taylor P C, Tamboli A C and Toberer E S 2014 Efficient route to phase selective synthesis of type II silicon clathrates with low sodium occupancy *CrystEngComm* **16** 3940–9

[24] Ammar A, Cros C, Pouchard M, Jaussaud N, Bassat J-M, Villeneuve G, Duttine M, Ménétrier

M and Reny E 2004 On the clathrate form of elemental silicon, Si_{136}: preparation and characterisation of Na_xSi_{136} ($x \rightarrow 0$) *Solid State Sci.* **6** 393–400

[25] Gryko J, McMillan P F, Marzke R F, Ramachandran G K, Patton D, Deb S K and Sankey O F 2000 Low-density framework form of crystalline silicon with a wide optical band gap *Phys. Rev. B* **62** R7707

[26] Blase X 2003 Quasiparticle band structure and screening in silicon and carbon clathrates *Phys. Rev. B* **67** 035211

[27] Adams G B, O'Keeffe M, Demkov A A, Sankey O F and Huang Y-M 1994 Wide-band-gap Si in open fourfold-coordinated clathrate structures *Phys. Rev. B* **49** 8048

[28] Dong J, Sankey O F and Kern G 1999 Theoretical study of the vibrational modes and their pressure dependence in the pure clathrate-II silicon framework *Phys. Rev. B* **60** 950

[29] Connétable D 2007 Structural and electronic properties of p-doped silicon clathrates *Phys. Rev. B* **75** 125202

[30] Martinez A D, Krishna L, Baranowski L L, Lusk M T, Toberer E S and Tamboli A C 2013 Synthesis of Group IV Clathrates for Photovoltaics *IEEE J. Photovolt.* **3** 1305–10

[31] Malone B D and Cohen M L 2012 Prediction of a metastable phase of silicon in the Ibam structure *Phys. Rev. B* **85** 024116

[32] Xiang H J, Huang B, Kan E, Wei S-H and Gong X G 2013 Towards direct-gap silicon phases by the inverse band structure design approach *Phys. Rev. Lett.* **110** 118702

[33] Zwijnenburg M A, Jelfs K E and Bromley S T 2010 An extensive theoretical survey of low-density allotropy in silicon *Phys. Chem. Chem. Phys.* **12** 8505–8512

[34] Kim D Y, Stefanoski S, Kurakevych O O and Strobel T A 2015 Synthesis of an open-framework allotrope of silicon *Nat. Mater.* **14** 169–73

[35] Kurakevych O O, Strobel T A, Kim D Y, Muramatsu T and Struzhkin V V 2013 Na-Si Clathrates Are High-Pressure Phases: A Melt-Based Route to Control Stoichiometry and Properties *Cryst. Growth Des.* **13** 303–7

[36] Bryan J D and Stucky G D 2001 $Eu_4Ga_8Ge_{16}$: A New Four-Coordinate Clathrate Network *Chem. Mater.* **13** 253–7

[37] Wosylus A, Prots Y, Burkhardt U, Schnelle W and Schwarz U 2007 High-pressure synthesis of the electron-excess compound $CaSi_6$ *Sci. Technol. Adv. Mater.* **8** 383–8

[38] Wosylus A, Prots Y, Burkhardt U, Schnelle W, Schwarz U and Grin Y 2014 High-pressure Synthesis of Strontium Hexasilicide *Z. Für Naturforschung B* **61** 1485–1492

[39] Wosylus A, Demchyna R, Prots Y, Schnelle W and Schwarz U 2014 Refinement of the crystal structure of barium hexasilicide, $BaSi_6$ *Z. Für Krist. - New Cryst. Struct.* **224** 347–348

[40] Wosylus A, Prots Y, Burkhardt U, Schnelle W, Schwarz U and Grin Y 2006 Breaking the Zintl rule: High-pressure synthesis of binary $EuSi_6$ and its ternary derivative $EuSi_{6-x}Ga_x$ ($0 \leqslant x \leqslant 0.6$) *Solid State Sci.* **8** 773–81

[41] Baerlocher C, McCusker L B and Olson D H 2007 *Atlas of zeolite framework types* (Elsevier)

[42] Arrieta U, Katcho N A, Arcelus O and Carrasco J 2017 First-Principles Study of Sodium Intercalation in Crystalline Na_x Si_{24} ($0 \leq x \leq 4$) as Anode Material for Na-ion Batteries *Sci. Rep.* **7**

[43] Linghu J, Shen L, Yang M, Xu S and Feng Y P 2017 Si_{24}: An Efficient Solar Cell Material *J. Phys. Chem. C*

[44] Lewis N S and Crabtree G 2005 *Basic Research Needs for Solar Energy Utilization: report of the Basic Energy Sciences Workshop on Solar Energy Utilization, April 18-21, 2005* ed N S Lewis, G Crabtree, A J Nozik, M R Wasielewski and P Alivisatos (Washington, DC: US Department of Energy, Office of Basic Energy Science)

[45] Ouyang T, Zhang P, Xiao H, Tang C, Li J, He C and Zhong J 2017 Potential thermoelectric material open framework Si_{24} from a first-principles study *J. Phys. Appl. Phys.*

[46] He Y, Lu X and Kim D Y 2018 A first-principles study on Si_{24} as an anode material for rechargeable batteries *RSC Adv.* **8** 20228–33

[47] Marzouk A, Balbuena P B and El-Mellouhi F 2016 Open Framework Allotropes of Silicon: Potential Anode Materials for Na and Li-ion Batteries *Electrochimica Acta* **207** 301–7

[48] Marzouk A, Soto F A, Burgos J C, Balbuena P B and El-Mellouhi F 2017 Dynamics of the Lithiation and Sodiation of Silicon Allotropes: From the Bulk to the Surface *J. Electrochem. Soc.* **164** A1644–50

[49] Guerette M, Strobel T A, Zhang H, Juhl S J, Alem N, Lokshin K, Krishna L and Taylor P C Advanced Synthesis of Na_4Si_{24} *MRS Adv.*

[50] Guerette M, Ward M D, Lokshin K A, Wong A T, Zhang H, Stefanoski S, Kurakevych O, Le Godec Y, Juhl S J, Alem N, Fei Y and Strobel T A 2018 Synthesis and Properties of Single-Crystalline Na_4Si_{24} *Cryst. Growth Des.*

[51] Anon JADE for XRD

[52] Bruker 2012 *APEX3* (Bruker AXS Inc., Madison, Wisconsin, USA)

[53] Sheldrick G M 1996 *SADABS* (University of Gottingen, Germany)

[54] Sheldrick G 2008 A short history of SHELX *Acta Crystallogr. Sect. A* **64** 112–22

[55] Sheldrick G 2015 Crystal structure refinement with SHELXL *Acta Crystallogr. Sect. C* **71** 3–8

[56] Gelato L M and Parthe E 1987 STRUCTURE TIDY - a computer program to standardize crystal structure data *J. Appl. Crystallogr.* **20** 139–43

[57] Parthe E and Gelato L M 1984 The standardization of inorganic crystal-structure data *Acta Crystallogr. Sect. A* **40** 169–83

[58] Palmer D 2015 *CrystalMaker* (Oxford, England: CrystalMaker Software Ltd.)

[59] Prescher C and Prakapenka V B 2015 DIOPTAS: a program for reduction of two-dimensional X-ray diffraction data and data exploration *High Press. Res.* **35** 223–30

[60] Anon AZtecEnergy - EDS software - Oxford Instruments

[61] Chen R-S, Tang C-C, Shen W-C and Huang Y-S 2015 Ohmic Contact Fabrication Using a Focused-ion Beam Technique and Electrical Characterization for Layer Semiconductor Nanostructures *J. Vis. Exp. JoVE*

[62] Chen R-S, Tang C-C, Shen W-C and Huang Y-S 2014 Thickness-dependent electrical conductivities and ohmic contacts in transition metal dichalcogenides multilayers *Nanotechnology* **25** 415706

[63] Perdew J P, Burke K and Ernzerhof M 1996 Generalized Gradient Approximation Made Simple *Phys. Rev. Lett.* **77** 3865–8

[64] Perdew J P and Wang Y 1992 Accurate and simple analytic representation of the electron-gas correlation energy *Phys. Rev. B* **45** 13244–9

[65] Kresse G and Furthmüller J 1996 Efficient iterative schemes for ab initio total-energy calculations using a plane-wave basis set *Phys. Rev. B* **54** 11169–86

[66] Heyd J, Scuseria G E and Ernzerhof M 2003 Hybrid functionals based on a screened Coulomb potential *J. Chem. Phys.* **118** 8207–15

[67] Paier J, Marsman M, Hummer K, Kresse G, Gerber I C and Ángyán J G 2006 Screened hybrid density functionals applied to solids *J. Chem. Phys.* **124** 154709

[68] Blöchl P E 1994 Projector augmented-wave method *Phys. Rev. B* **50** 17953–79

[69] Gajdoš M, Hummer K, Kresse G, Furthmüller J and Bechstedt F 2006 Linear optical properties in the projector-augmented wave methodology *Phys. Rev. B* **73** 045112

[70] Chae K, Kang S-H, Choi S-M, Kim D Y and Son Y-W 2018 Enhanced Thermoelectric Properties in a New Silicon Crystal Si_{24} with Intrinsic Nanoscale Porous Structure *Nano Lett.* **18** 4748–54

[71] Soref R and Bennett B 1987 Electrooptical effects in silicon *IEEE J. Quantum Electron.* **23** 123–9

[72] Spitzer W and Fan H Y 1957 Infrared Absorption in n-Type Silicon *Phys. Rev.* **108** 268–71

[73] Spitzer W G and Whelan J M 1959 Infrared Absorption and Electron Effective Mass in n - Type Gallium Arsenide *Phys. Rev.* **114** 59–63

[74] Tauc J 1968 Optical properties and electronic structure of amorphous Ge and Si *Mater. Res. Bull.* **3** 37–46

[75] Tauc J, Grigorovici R and Vancu A 2006 Optical Properties and Electronic Structure of Amorphous Germanium *Phys. Status Solidi B* **15** 627–37

[76] Schmid P E 1981 Optical absorption in heavily doped silicon *Phys. Rev. B* **23** 5531–6

[77] Lush G B, Melloch M R, Lundstrom M S, MacMillan H F and Asher S 1993 Concentration-dependent optical-absorption coefficient in n-type GaAs *J. Appl. Phys.* **74** 4694–702

[78] Himeno R, Kume T, Ohashi F, Ban T and Nonomura S 2013 Optical absorption properties of Na_xSi_{136} clathrate studied by diffuse reflection spectroscopy *J. Alloys Compd.* **574** 398–401

[79] Krishna L, Martinez A D, Baranowski L L, Brawand N P, Koh C A, Stevanović V, Lusk M T, Toberer E S and Tamboli A C 2014 Group IV clathrates: synthesis, optoelectonic properties, and photovoltaic applications vol 8981 pp 898108-898108–11

[80] Baranowski L L, Krishna L, Martinez A D, Raharjo T, Stevanović V, Tamboli A C and Toberer E S 2014 Synthesis and optical band gaps of alloyed Si–Ge type II clathrates *J Mater Chem C* **2** 3231–7

[81] Fox M 2002 Optical properties of solids

[82] Spitzer W G and Fan H Y 1957 Determination of Optical Constants and Carrier Effective Mass of Semiconductors *Phys. Rev.* **106** 882–90

[83] Li S S and Thurber W R 1977 The dopant density and temperature dependence of electron mobility and resistivity in n-type silicon *Solid-State Electron.* **20** 609–16

[84] Bi Y, Xu E, Strobel T A and Li T 2018 Formation of inclusion type silicon phases induced by inert gases *Commun. Chem.* **1** 1–9